

Interaction induced point scatterer lattices and flat band condensation of exciton-polaritons

S. Alyatkin,¹ H. Sigurdsson,^{2,1} A. Askitopoulos,¹ J. D. Töpfer,^{2,1} and P. G. Lagoudakis^{1,2,*}

¹*Skolkovo Institute of Science and Technology, Moscow, Bolshoy Boulevard 30, bld. 1, 121205, Russia*

²*School of Physics and Astronomy, University of Southampton, Southampton, SO17 1BJ, United Kingdom*

(Dated: April 22, 2022)

One of the recently established paradigms in the study of condensed matter physics is examining a system's behaviour in artificially constructed potentials. This allows one to obtain insight on a range of physical phenomena which may require non-feasible or hardly achievable experimental conditions. Here, we devise and implement an all-optical approach to a system of exciton-polaritons in semiconductor microcavities to load the particles into desired periodic potentials. We demonstrate a two-dimensional system of polariton condensates in two regimes - lattices of point scatterers, and confined states through non-resonant pumping with Gaussian beams arranged in a conventional, and an inverse Lieb configuration. We utilize energy tomography on the coherent polariton emission to reveal the intricate band structure of polaritonic Lieb lattices, and report on fully optically generated polariton condensation in S-, and dispersionless P-band states.

Introduction — Artificial lattices are highly attractive not only for obtaining insight into properties of crystal structures in the solid state, but also for creating patterned structures not found in nature. They can be used to investigate spin frustration in triangular geometries, massless Dirac fermions in honeycomb structures, and strongly correlated states in dispersionless flat bands [1]. A prominent example is the two-dimensional (2D) edge-centered square (Lieb) lattice [2] which hosts an excess of phenomena including topological phases, dispersionless flat bands, and Dirac points [3–5]. As such, the Lieb lattice, along with the honeycomb and kagome lattices, has become a popular testbed in controllable experimental conditions to explore difficult-to-reach lattice physics. Each site in such a lattice serves as an artificial attractive potential for particles (i.e., an “atom” for an “electron”). The Lieb lattice in a tight-binding picture has been realized for various systems such as electrons [6, 7], photons [8–10], cold atoms [11], and exciton-polaritons [12–15].

In contrast to lattices of tightly confined waves there exists the inverse, and less experimentally studied case, of coherent matter-wave scattering in lattices made up of small (less or equal to the particle de Broglie wavelength) repulsive non-Hermitian potentials. Since the early work of Kronig and Penney [16], an ordered arrangement of spherically symmetric scatterers is known to give rise to bands and bandgaps. The study of elastic scattering of incoming and outgoing states on a static object is at the heart of electromagnetic-, Schrödinger-, and sound-wave scattering theory [17]. However, the realization of non-Hermitian scatterer lattices for strongly nonlinear matter-waves with coherence length exceeding the scatterer spacing is, to date, a mostly unexplored area.

Semiconductor microcavities in the strong light-matter coupling regime are especially appealing for engineering artificial lattices as they host matter-wave quasi-

particle modes known as exciton-polaritons (from here on *polaritons*) [18]. These modes possess very strong nonlinearities and permit easy imprinting and extraction of information through the leaky cavity photon field, making them favorable candidates to study optical many-body hydrodynamic phenomena [19, 20], topological phases [21, 22], and implementation of information processing [23, 24]. Moreover, these strong nonlinearities result in repulsion of condensate particles from the background uncondensed particles, co-localized with the pumped area [25, 26]. This enables all-optical design of a potential landscape for polaritons [27–31], in close analogy to dipole optical traps for cold atoms [32] or photorefractive crystals [33]. The potential landscape in optically imprinted polaritonic lattices is directly proportional to the excitation intensity and thus determined by arrangement of Gaussian shaped pump spots. However,

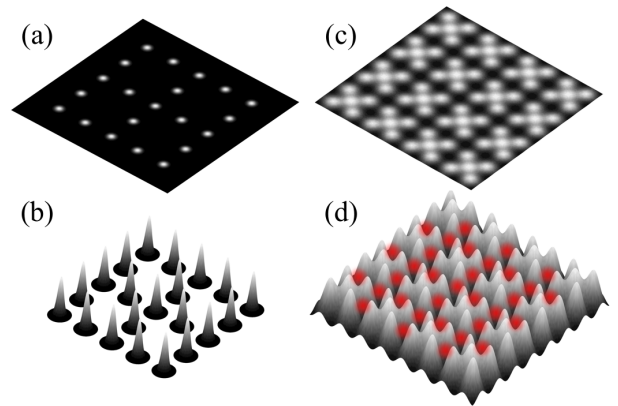


Figure 1. (a) Spatial excitation intensity profile of Gaussian spots arranged in a Lieb lattice. (b) Corresponding potential landscape with polariton condensation occurring on the maxima of repulsive potentials. (c) Inverse Lieb lattice of closely spaced Gaussian pumps leading to potential minima in a Lieb pattern, shown in (d). The polaritons localise in these potential minima, schematically shown with red colour.

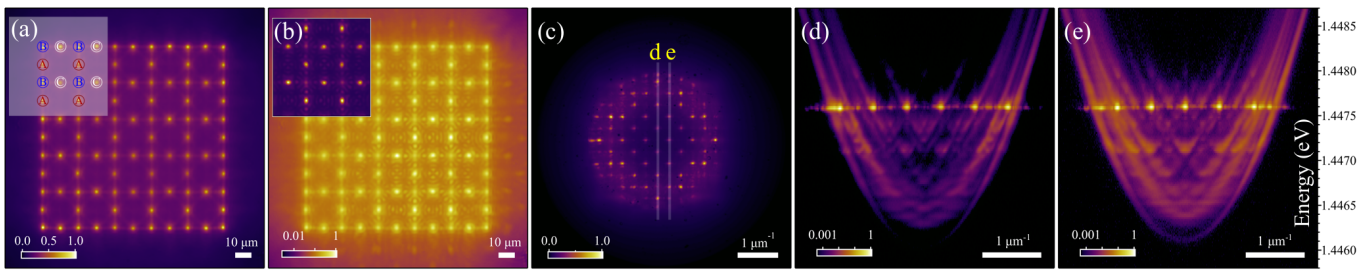


Figure 2. (a) Optical lattice of 96 polariton condensates at threshold arranged in a Lieb geometry with a lattice constant set to $D = 22.3 \mu\text{m}$. The inset in (a) schematically shows sublattices denoted with letters A,B,C forming the Lieb lattice. (b) Real space polariton PL for the lattice pumped at $P = 1.1P_{\text{thr}}$. Driving the system above threshold leads to the condensation on A and C sublattices, see inset shown in linear colorscale. (c) Momentum space polariton PL for $P = 1.1P_{\text{thr}}$. Semi-transparent thin lines denoted with yellow letters “d” and “e” correspond to $k_x = 0$ and $k_x = 2\pi/D$, for which the energy-resolved momentum space PL shown in (d),(e) respectively.

by changing the lattice topology, size of the unit cell, or potential strength one can move from the lattice of attractive (confining) potentials to a lattice of repulsive (scatterers) potentials without any irreversible effects on the sample, as shown schematically in Fig. 1. This flexibility in tuning the lattice properties through excitation structuring makes a system of microcavity polaritons appealing to access various lattice physics in a recyclable setting. Obviously, the polariton condensate generated by the lasers is sensitive to energy landscape felt by the particles. Condensate polaritons can experience localisation in the minima of the potential landscape [34] (see Figs. 1(c,d)), while on the other hand they can also localize on the maxima of the potentials [35] (see Figs. 1(a,b)). In the former case, the system e.g. shares analogies with 2D electron transport, whereas in the latter case with a planar photonic crystal with air hole patterning in a dielectric medium [36].

In this work, we experimentally demonstrate optically imprinted both tunable repulsive (Fig. 1(a,b)) and attractive (Fig. 1(c,d)) Lieb lattices populated by a macroscopic polariton condensate. In other words, by only optical means we engineer and study first, a paradigmatic matter-wave scatterer lattice with rich band structure, and second, a polariton tight-binding lattice possessing flat band states. The latter is known to have suppressed kinetic energy and strongly interacting phases with high sensitivity to potential perturbations [37]. Non-resonant injection (by arrangement of Gaussian laser beams) of free charge carriers and their subsequent relaxation towards the polaritonic bands makes possible full momentum-energy space tomography to scrutinize the details of the engineered band structure. Measurements of the real space polariton photoluminescence (PL) provide direct access to the macroscopically occupied state, which is confirmed by corresponding Bloch state analysis. The quality of our approach is further evidenced by direct observation of S- and dispersionless P-band condensation in an attractive Lieb lattice. This is achieved by pumping the system with thoroughly shaped

excitation profile, forming an inverse Lieb lattice in the same spirit as the vacancy lattice created in electronic systems [6, 7] or optical lattices for cold atoms [38, 39].

Results — A strain compensated 2λ GaAs-based planar microcavity with embedded three pairs of $\text{In}_{0.08}\text{Ga}_{0.92}\text{As}$ quantum wells [40] is held at ≈ 4 K in a closed-cycle helium cryostat. The non-resonant excitation (single mode laser emission at 1.5578 eV, at an exciton-photon detuning of -4 meV) is chopped at a frequency of 5 kHz (duty cycle 1%) with an acousto-optical modulator to avoid sample heating. A desired pump profile is shaped by a computer-controlled reflective phase only spatial light modulator [41] and projected onto the sample through a microscope objective (NA=0.42). We collect the real space polariton PL in transmission geometry and spectrally filter it from the excitation laser. We define the horizontal and vertical momentum space coordinates as $\mathbf{k} = (k_x, k_y)$.

In Fig. 2(a) we show an optically pumped lattice of 96 polariton condensates at threshold power ($P \approx P_{\text{thr}}$) arranged into a scatterer Lieb geometry. The size (FWHM) of the Gaussian laser spots sustaining the condensates is $\approx 2 \mu\text{m}$ and the lattice constant is set to $D \approx 22.3 \mu\text{m}$. As shown in inset in Fig. 2(a), the Lieb lattice is composed of three overlaid square sublattices schematically denoted with A, B, and C letters. Being close to threshold, the condensates spatial coherence does not extend outside their respective pump spot [42] making them effectively isolated objects. Figures 2(b) and (c) show the real and momentum space polariton PL above threshold ($P = 1.1P_{\text{thr}}$), while Figs. 2(d,e) show energy-momentum space PL at $k_x = 0$ and $k_x = 2\pi/D$ respectively. Driving the system above threshold increases both the coherence and particle outflow from each condensate resulting in the appearance of interference fringes between the radiating condensates as well as Bragg diffraction peaks in momentum space. The inset in Fig. 2(b) shows a cropped region of the same panel, plotted in linear colorscale for comparison. Interestingly, the state excited in Figs. 2(b-e) corresponds to an excited Bloch state of partial de-

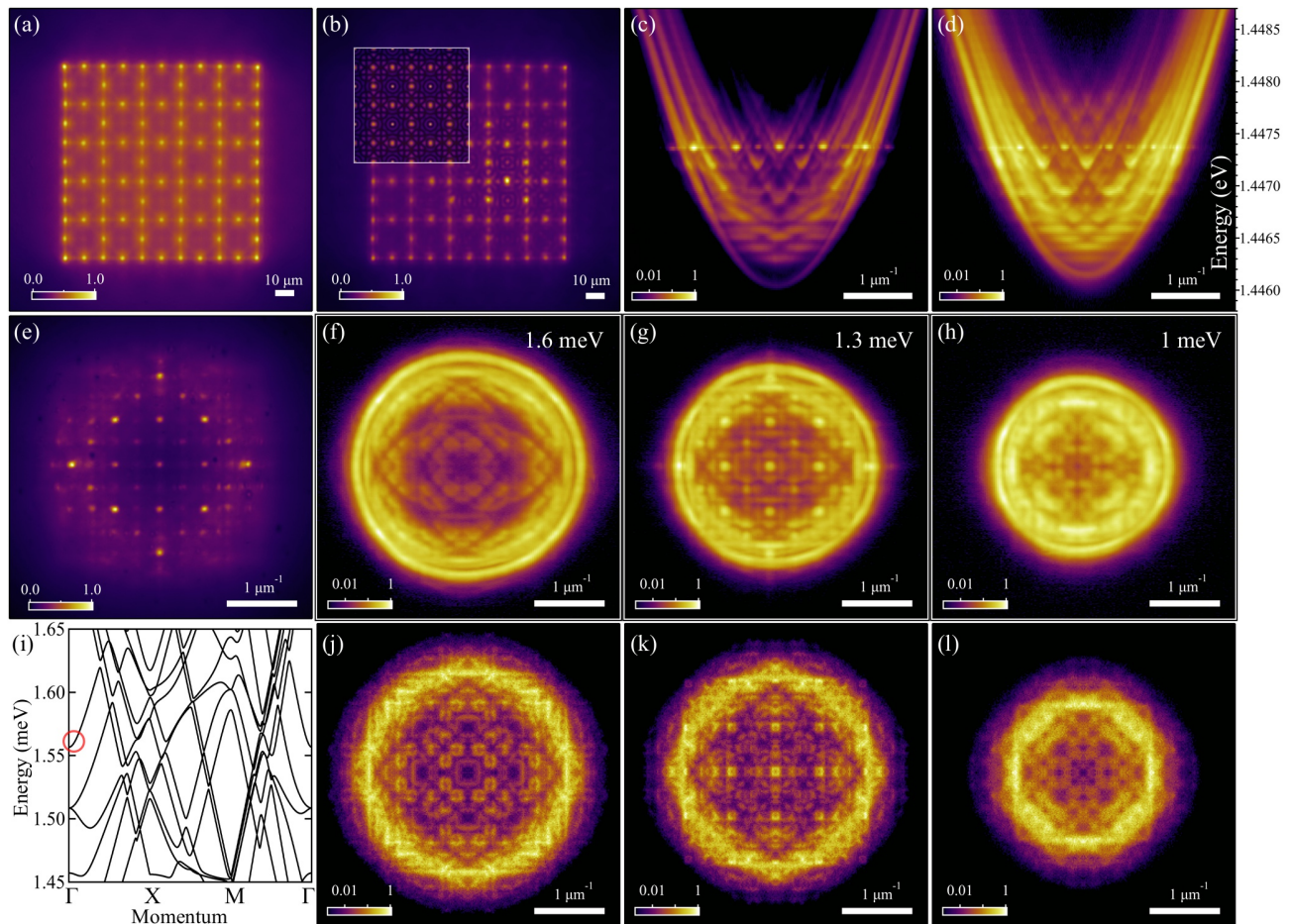


Figure 3. (a) Optical Lieb lattice of polariton condensates with a lattice constant set to $D = 20.3 \mu\text{m}$ excited at $P \approx P_{\text{thr}}$ and (b) at $P = 1.2P_{\text{thr}}$, an inset shows calculated Bloch state intensity for comparison. (c,d) Energy-resolved momentum space polariton PL at $P = 1.2P_{\text{thr}}$ for $k_x=0$ and $k_x = 2\pi/D$ respectively. (e) Integrated over all energies momentum space polariton PL at $P = 1.2P_{\text{thr}}$, and (f,g,h) energy-resolved “slices” of momentum space at energy of 1.6 meV, 1.3 meV and 1 meV with respect to the bottom of lower polariton branch. (i) Calculated bands with red circle, corresponding to inset in (b). (j,k,l) Calculated “slices” of polariton momentum space PL.

structive interference at sublattice B (clearly visible from the inset). This is due to polaritons relaxing into the high symmetry Γ -points of the bands [43, 44] which are located at $\mathbf{k} = 2\pi(n_x, n_y)/D$ where $n_x, n_y \in \mathbb{Z}$ as can be seen from the sharp Bragg peaks in the reciprocal domain. The partial destructive interference corresponds to superposition waves with momenta at points where $|n_x - n_y| \in \{2n + 1 | n \in \mathbb{N}\}$ as can be seen from Fig. 2(c). In fact, a complete destructive interference should occur at sublattice B but instead becomes partially compensated due the strong particle gain from the pump spot, an inherently nonlinear effect of the driven-dissipative condensate system. We note that the illuminated bands in Figs. 2(d,e) show that polaritons in the repulsive Lieb lattice experience crystal scattering. We also observed band-structure formation for the square scatterer lattice of 5×5 polariton condensates with a similar lattice constant (see SM).

In Fig. 3 we show results for the scatterer Lieb lat-

tice for a slightly smaller lattice constant $D = 20.3 \mu\text{m}$. By changing the lattice constant only by 9% we observe condensation into a different excited Bloch state, underlining the tunability of our approach to access different excited modes. The system in Fig. 3(a) and in Figs. 3(b-h) is pumped at ($P \approx P_{\text{thr}}$) and above ($P = 1.2P_{\text{thr}}$) threshold respectively. Figures 3(a,b) show the real space polariton PL, Figs. 3(c,d) show energy-resolved momentum space PL at $k_x = 0$ and $k_x = 2\pi/D$ respectively showing clear band formation. Unlike Fig. 2, here we observe an excited Bloch state condensate with constructive interference between all sublattice cells. This corresponds to Bloch momenta lying at points satisfying $|n_x - n_y| \in \{2n | n \in \mathbb{N}\}$ as can be seen from the location of the diffraction peaks in Fig. 3(e). Next, by scanning a Fourier space PL image across a slit of a spectrometer with a motorized mount, we reconstruct energy-resolved “slices” of momentum space PL at three specific energies, see Figs. 3(f-h). The applied energy tomography reveals

the full picture of complex band formation. We also calculate the band structure using two distinct methods: Bloch analysis, and Monte-Carlo sampling of the polariton Schrödinger equation. The results shown in Fig. 3(i) and Figs. 3(j-l) respectively, are in good agreement with experiment, (see SM for details). The observed diversity of the states symmetry in repulsive Lieb potentials differs dramatically from the natural square geometry (see SM).

In Fig. 4 we show a conventional Lieb lattice where the non-resonant excitation is arranged to form a Lieb lattice of potential minima [see Figs. 4(a,f)]. This type of optical trapping has been exploited before to achieve condensation of polaritons into the low energy trap states away from the pump spots [26, 34]. It is worth noting that the polariton condensates, tightly-bound in the potential minima, interact here via tunneling (evanescent wave transport) in analogy to conventional condensed matter systems, while the condensates localised on top of the repulsive potentials in Fig. 2 and Fig. 3 interact via non-evanescent ballistic transport [35] in close analogy to externally coupled laser systems. Figure 4(a) shows the excitation pattern with $D = 13 \mu\text{m}$, Figs. 4(b,c) real space polariton PL below and above threshold respectively. The observations reveal polaritons accumulating in the ground state of the lattice of potentials, giving rise to the collective S-band ground state. By adjusting the lattice constant, the optimal condensate gain can be shifted to a different Bloch state. Figures 4(f-h) show the same measurements but now for $D = 16 \mu\text{m}$ with all pumps having equal intensity. The real space polariton PL in Fig. 4(h) demonstrates clear localization of the P-orbitals into sublattices A and C, whereas at sublattice B destructive interference occurs. This state belongs to a dispersionless P-flatband [12, 13] in the Lieb lattice and is the first evidence of polariton condensation into optically generated flatband states.

Experimentally implemented energy tomography measurements shown in Figs. 4(n,o), and calculated band structure shown in Figs. 4(k,l,m), confirms that the dominant condensate mode of the system belongs to the dispersionless P-flatband. This can be seen from the integrated momentum space PL in Fig. 4(i) which exhibits a similar intensity pattern obtained from calculation of the polariton modes belonging to the P-flatband [see Fig. 4(l) and the band marked l in Fig. 4(k)]. This agreement is enhanced when the polariton PL is energy-resolved, revealing sharper intensity features in Fig. 4(n), matching calculated ones. We also investigate the lowest energy P-band denoted by letter m in Fig. 4(k) with calculated and experimentally observed intensity pattern shown in Figs. 4(m,o) respectively, revealing sharp degenerate momentum space lines. Interestingly, we also observe symmetry breaking in energy-resolved momentum space, see inset in Fig. 4(o). This observation could be evidence of strongly interacting particle phase, inherent to a flat

band state [37]. We confirmed the absence of similar symmetry breaking manifestations for all other bands populated by polaritons. Two “faulty” spots in the excitation pattern in Fig. 4(f) (in the first top row and the first left column) can be caused by optical aberrations due to defects or interference with higher diffraction orders of the spatial light modulator. We believe that the presented optical approach is a powerful technique to design and shape artificial potentials in 2D systems.

To better understand why condensation favors the P-flatband in Fig. 4(h) one needs to appreciate that the excitation geometry creates slightly elliptical confinement at sublattices A and C which splits the energies and linewidths of the $P_{x,y}$ orbitals. In other words, the overlap of $P_{x,y}$ orbitals into the pumping (gain) region is different. For sublattice A (C) the P_x (P_y) orbital overlaps more with the pump. Since the rate of polariton scattering from the background reservoir into the condensate mode is directly proportional to its overlap with the pump region it results in a dominant P-flatband condensation with $P_{x,y}$ orbitals at sublattices A,C respectively. Our interpretation is supported through a non-Hermitian tight-binding theory (see SM).

Discussion and conclusions— The demonstrated optically arranged system of exciton-polaritons presents a flexible platform to study fundamental proposals on non-Hermitian phenomena in artificial lattices including nonlinear reshaping of the crystal bands when above condensation threshold. In Figs. 2-3 we have demonstrated the condensation of polaritons into excited Bloch states belonging to a lattice of scatterers (narrow waist repulsive potentials) shaped into a Lieb pattern. The observed crystal bands and agreement with theoretical models opens up a path to explore more intriguing effects of scattered matter-waves such as slow polaritons [45], guided polaritons [46], and solitonic modes [47].

In Fig. 4 we have demonstrated the inverse case of tightly bound polariton waves in a Lieb lattice of optically induced attractive potentials with condensation into flat band states. Given the strong nonlinear nature of exciton-polaritons, condensation into a flat band state opens a window to investigate strongly correlated states of matter and the effects of disorder against interactions [48]. We point out that the current study is performed in the scalar polariton regime, but can be easily extended to include its spin degree of freedom by changing the pump polarization. The implemented energy tomography methods provide complete access to the polariton states in Fourier space and can be used to study reshaping of the spectrum under arbitrary lattice deformation and nonlinear effects. Furthermore, bands induced by our optically engineered landscape can be populated using resonant excitation permitting study of the evolution of polariton matter waves in a moldable optical potential with arbitrary momentum and frequency.

Acknowledgements — We acknowledge the support of

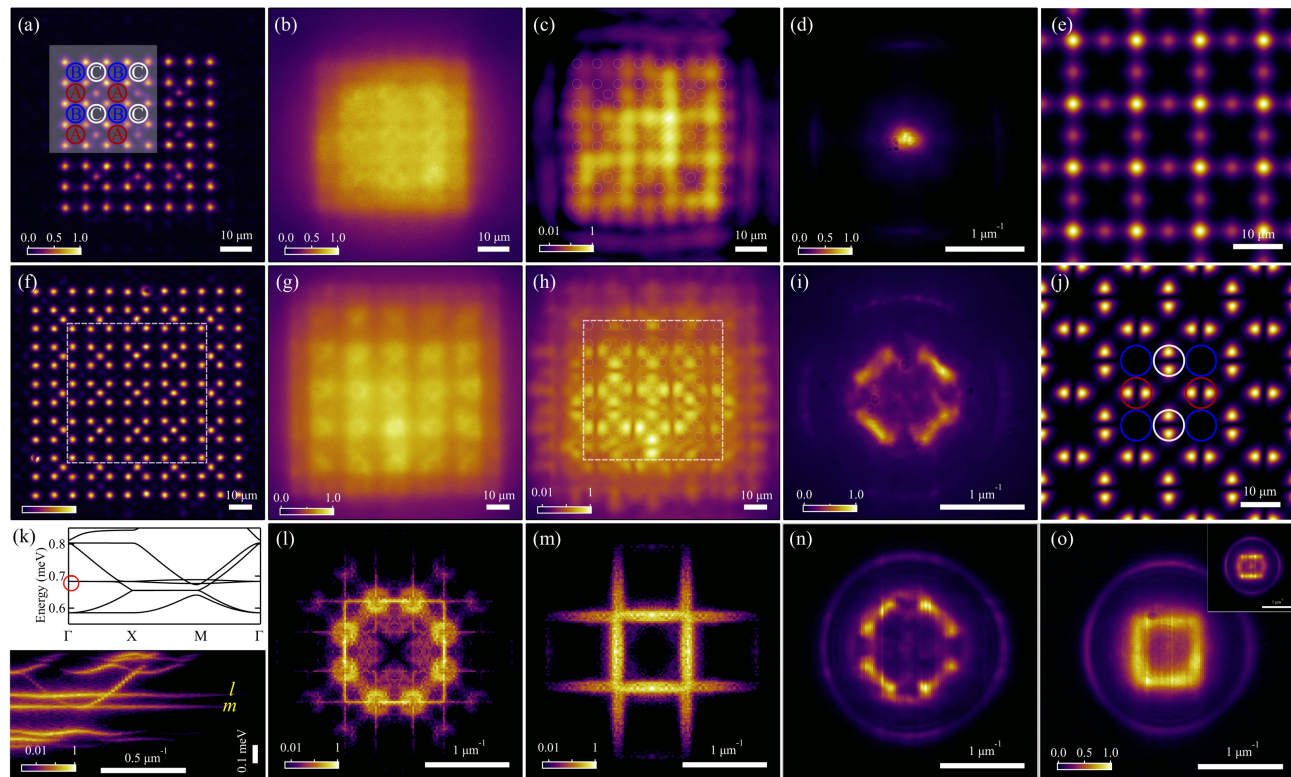


Figure 4. (a,f) Pumping profile of Gaussian spots arranged in the inverse Lieb geometry with lattice constants $D = 13 \mu\text{m}$ and $16 \mu\text{m}$ respectively. In (a) the cube-centered spots are 40% weaker in intensity compared to the rest of the pump spots. In (f) all spots are equally intense. (b,g) Real space polariton PL below condensation threshold. (c,h) Real and (d,i) momentum space PL above condensation threshold with a pattern corresponding to the S-band ground state and P-flatband state, respectively. White circles in (c) and (h) denote the pumps positions. (e,g) Calculated real space Bloch state intensities belonging to the S-orbital lowest band and P-orbital flatband state respectively, matching experimentally measured polariton PL. Colourful circles in (a) and (j) denote unit cell of conventional Lieb lattice. (k) Calculated bands belonging to P-orbital states (top) and calculated dispersion (bottom) at $k_x = 2\pi/D$ for the system pumped with an excitation profile (f). (l,m) Calculated energy-resolved “slices” of momentum space PL, corresponding to energies marked with letters l and m in (k), which denote the P-flatband and the lowest energy P-band respectively. Corresponding experimentally extracted momentum space “slices” (n,o) confirm polariton condensation in P-flatband state. An inset in (o) shows observed symmetry breaking in momentum space for the lattice constant increased only by 1%.

the UK’s Engineering and Physical Sciences Research Council (grant EP/M025330/1 on Hybrid Polaritonics), the RFBR projects No. 20-52-12026 (jointly with DFG) and No. 20-02-00919.

* Pavlos.Lagoudakis@soton.ac.uk

- [1] M. Polini, F. Guinea, M. Lewenstein, H. C. Manoharan, and V. Pellegrini, *Nature Nanotechnology* **8**, 625 (2013).
- [2] E. H. Lieb, *Phys. Rev. Lett.* **62**, 1201 (1989).
- [3] C. Weeks and M. Franz, *Phys. Rev. B* **82**, 085310 (2010).
- [4] N. Goldman, D. F. Urban, and D. Bercioux, *Phys. Rev. A* **83**, 063601 (2011).
- [5] M. Niță, B. Ostahie, and A. Aldea, *Phys. Rev. B* **87**, 125428 (2013).
- [6] R. Drost, T. Ojanen, A. Harju, and P. Liljeroth, *Nature Physics* **13**, 668 (2017).
- [7] M. R. Slot, T. S. Gardenier, P. H. Jacobse, G. C. P. van Miert, S. N. Kempkes, S. J. M. Zevenhuizen, C. M. Smith, D. Vanmaekelbergh, and I. Swart, *Nature Physics* **13**, 672 (2017).
- [8] D. Guzmán-Silva, C. Mejía-Cortés, M. A. Bandres, M. C. Rechtsman, S. Weimann, S. Nolte, M. Segev, A. Szameit, and R. A. Vicencio, *New Journal of Physics* **16**, 063061 (2014).
- [9] S. Mukherjee, A. Spracklen, D. Choudhury, N. Goldman, P. Öhberg, E. Andersson, and R. R. Thomson, *Phys. Rev. Lett.* **114**, 245504 (2015).
- [10] R. A. Vicencio, C. Cantillano, L. Morales-Inostroza, B. Real, C. Mejía-Cortés, S. Weimann, A. Szameit, and M. I. Molina, *Phys. Rev. Lett.* **114**, 245503 (2015).
- [11] S. Taie, H. Ozawa, T. Ichinose, T. Nishio, S. Nakajima, and Y. Takahashi, *Science Advances* **1** (2015), 10.1126/sciadv.1500854.
- [12] S. Klemmt, T. H. Harder, O. A. Egorov, K. Winkler, H. Suchomel, J. Beierlein, M. Emmerling, C. Schneider, and S. Höfling, *Applied Physics Letters* **111**, 231102 (2017).

- [13] C. E. Whittaker, E. Cancellieri, P. M. Walker, D. R. Gulevich, H. Schomerus, D. Vaitiekus, B. Royall, D. M. Whittaker, E. Clarke, I. V. Iorsh, I. A. Shelykh, M. S. Skolnick, and D. N. Krizhanovskii, *Phys. Rev. Lett.* **120**, 097401 (2018).
- [14] V. Goblot, B. Rauer, F. Vicentini, A. Le Boité, E. Galopin, A. Lemaître, L. Le Gratiet, A. Harouri, I. Sagnes, S. Ravets, C. Ciuti, A. Amo, and J. Bloch, *Phys. Rev. Lett.* **123**, 113901 (2019).
- [15] T. H. Harder, O. A. Egorov, J. Beierlein, P. Gagel, J. Michl, M. Emmerling, C. Schneider, U. Peschel, S. Höfling, and S. Klemmt, arXiv e-prints, arXiv:2002.05405 (2020), arXiv:2002.05405 [cond-mat.mes-hall].
- [16] R. D. L. Kronig, W. G. Penney, and R. H. Fowler, *Proceedings of the Royal Society of London. Series A, Containing Papers of a Mathematical and Physical Character* **130**, 499 (1931).
- [17] R. G. Newton, *Scattering Theory of Waves and Particles* (Springer-Verlag Berlin Heidelberg, 1982).
- [18] A. Kavokin, J. J. Baumberg, G. Malpuech, and F. P. Laussy, *Microcavities* (OUP Oxford, 2007).
- [19] P. Stepanov, I. Amelio, J.-G. Rousset, J. Bloch, A. Lemaître, A. Amo, A. Minguzzi, I. Carusotto, and M. Richard, *Nature Communications* **10**, 3869 (2019).
- [20] D. G. Suárez-Forero, V. Ardizzone, S. F. Covre da Silva, M. Reindl, A. Fieramosca, L. Polimeno, M. D. Giorgi, L. Dominici, L. N. Pfeiffer, G. Gigli, D. Ballarini, F. Laussy, A. Rastelli, and D. Sanvitto, *Light: Science & Applications* **9**, 85 (2020).
- [21] S. Klemmt, T. H. Harder, O. A. Egorov, K. Winkler, R. Ge, M. A. Bandres, M. Emmerling, L. Worschech, T. C. H. Liew, M. Segev, C. Schneider, and S. Höfling, *Nature* **562**, 552 (2018).
- [22] A. Gianfrate, O. Bleu, L. Dominici, V. Ardizzone, M. De Giorgi, D. Ballarini, G. Lerario, K. W. West, L. N. Pfeiffer, D. D. Solnyshkov, D. Sanvitto, and G. Malpuech, *Nature* **578**, 381 (2020).
- [23] A. V. Zasedatelev, A. V. Baranikov, D. Urbonas, F. Scafirimuto, U. Scherf, T. Stöferle, R. F. Mahrt, and P. G. Lagoudakis, *Nature Photonics* **13**, 378 (2019).
- [24] A. Opala, S. Ghosh, T. C. Liew, and M. Matuszewski, *Phys. Rev. Applied* **11**, 064029 (2019).
- [25] E. Wertz, L. Ferrier, D. D. Solnyshkov, R. Johne, D. Sanvitto, A. Lemaître, I. Sagnes, R. Grousson, A. V. Kavokin, P. Senellart, G. Malpuech, and J. Bloch, *Nature Physics* **6**, 860 (2010).
- [26] A. Askitopoulos, H. Ohadi, A. V. Kavokin, Z. Hatzopoulos, P. G. Savvidis, and P. G. Lagoudakis, *Phys. Rev. B* **88**, 041308 (2013).
- [27] G. Tosi, G. Christmann, N. G. Berloff, P. Tsotsis, T. Gao, Z. Hatzopoulos, P. G. Savvidis, and J. J. Baumberg, *Nature Physics* **8**, 190 (2012).
- [28] G. Tosi, G. Christmann, N. G. Berloff, P. Tsotsis, T. Gao, Z. Hatzopoulos, P. G. Savvidis, and J. J. Baumberg, *Nature Communications* **3**, 1 (2012).
- [29] N. G. Berloff, M. Silva, K. Kalinin, A. Askitopoulos, J. D. Töpfer, P. Cilibrizzi, W. Langbein, and P. G. Lagoudakis, *Nature Materials* **16**, 1120 (2017).
- [30] S. Alyatkin, J. D. Töpfer, A. Askitopoulos, H. Sigurdsson, and P. G. Lagoudakis, *Phys. Rev. Lett.* **124**, 207402 (2020).
- [31] L. Pickup, H. Sigurdsson, J. Ruostekoski, and P. G. Lagoudakis, arXiv e-prints, arXiv:2001.07616 (2020), arXiv:2001.07616 [cond-mat.mes-hall].
- [32] I. Bloch, *Nature Physics* **1**, 23 (2005).
- [33] D. N. Neshev, T. J. Alexander, E. A. Ostrovskaya, Y. S. Kivshar, H. Martin, I. Makasyuk, and Z. Chen, *Phys. Rev. Lett.* **92**, 123903 (2004).
- [34] H. Ohadi, Y. del Valle-Inclan Redondo, A. J. Ramsay, Z. Hatzopoulos, T. C. H. Liew, P. R. Eastham, P. G. Savvidis, and J. J. Baumberg, *Phys. Rev. B* **97**, 195109 (2018).
- [35] J. D. Töpfer, H. Sigurdsson, L. Pickup, and P. G. Lagoudakis, *Communications Physics* **3**, 2 (2020).
- [36] Y. Akahane, T. Asano, B.-S. Song, and S. Noda, *Nature* **425**, 944 (2003).
- [37] D. Leykam, A. Andreanov, and S. Flach, *Advances in Physics: X* **3** (2018), 10.1080/23746149.2018.1473052.
- [38] R. Shen, L. B. Shao, B. Wang, and D. Y. Xing, *Phys. Rev. B* **81**, 041410 (2010).
- [39] C. Gross and I. Bloch, *Science* **357**, 995 (2017).
- [40] P. Cilibrizzi, A. Askitopoulos, M. Silva, F. Bastiman, E. Clarke, J. M. Zajac, W. Langbein, and P. G. Lagoudakis, *Applied Physics Letters* **105**, 191118 (2014).
- [41] J. D. Töpfer, I. Chatzopoulos, H. Sigurdsson, T. Cookson, Y. G. Rubo, and P. G. Lagoudakis, in preparation (2020).
- [42] G. Roumpos, M. Lohse, W. H. Nitsche, J. Keeling, M. H. Szymańska, P. B. Littlewood, A. Löffler, S. Höfling, L. Worschech, A. Forchel, and Y. Yamamoto, *Proceedings of the National Academy of Sciences* **109**, 6467 (2012).
- [43] C. W. Lai, N. Y. Kim, S. Utsunomiya, G. Roumpos, H. Deng, M. D. Fraser, T. Byrnes, P. Recher, N. Kumada, T. Fujisawa, and Y. Yamamoto, *Nature* **450**, 529 (2007).
- [44] N. Y. Kim, K. Kusudo, C. Wu, N. Masumoto, A. Löffler, S. Höfling, N. Kumada, L. Worschech, A. Forchel, and Y. Yamamoto, *Nature Physics* **7**, 681 (2011).
- [45] T. Baba, *Nature Photonics* **2**, 465 (2008).
- [46] A. Mekis, J. C. Chen, I. Kurland, S. Fan, P. R. Villeneuve, and J. D. Joannopoulos, *Phys. Rev. Lett.* **77**, 3787 (1996).
- [47] A. Blanco-Redondo, C. Husko, D. Eades, Y. Zhang, J. Li, T. F. Krauss, and B. J. Eggleton, *Nature Communications* **5**, 3160 (2014).
- [48] F. Baboux, L. Ge, T. Jacqmin, M. Biondi, E. Galopin, A. Lemaître, L. Le Gratiet, I. Sagnes, S. Schmidt, H. E. Türeci, A. Amo, and J. Bloch, *Phys. Rev. Lett.* **116**, 066402 (2016).

Supplemental Material

SQUARE LATTICE OF SCATTERERS

In Fig. S1(a) we show an optically pumped polariton condensates lattice arranged into a scatterer square geometry for comparison against the Lieb geometry presented in Fig. 2 in the main text. Just like in the main text, we define the real space horizontal and vertical coordinates as $\mathbf{r} = (x, y)$, and in momentum space $\mathbf{k} = (k_x, k_y)$. The full-width-half-maximum (FWHM) of the Gaussian lasers sustaining the condensates is $\text{FWHM} \approx 2 \mu\text{m}$. The distance between the Gaussian pumps is set to $D \approx 22.5 \mu\text{m}$. The power of the excitation is approximately at threshold ($P \approx P_{\text{thr}}$). In Fig. S1(b) we show the corresponding energy-momentum space PL along $k_x = 0$. In Fig. S1(c,d) we show the same measurements but pumped further above condensation threshold ($P \approx 1.3P_{\text{thr}}$) which results in clearer appearance of interference fringes between the radiating condensates. From Fig. S1(b,d) we observe illuminated high energy bands within the lower polariton dispersion verifying that polaritons in the system experience crystal scattering.

THEORY OF POLARITON DYNAMICS

We consider the two-dimensional (2D) Schrödinger equation which describes a polariton in the static potential landscape designed by our optical non-resonant lasers.

$$i\hbar \frac{d\Psi}{dt} = [\hat{E} + V(\mathbf{r})] \Psi \quad (\text{S1})$$

Here, \hat{E} is the dispersion of the lower polariton branch. The upper polariton branch is neglected because it is both far away in energy and weakly populated by our experimental excitation scheme. Given the much larger effective mass of the excitons compared to the cavity photons we can set their dispersion to zero and the lower polariton dispersion

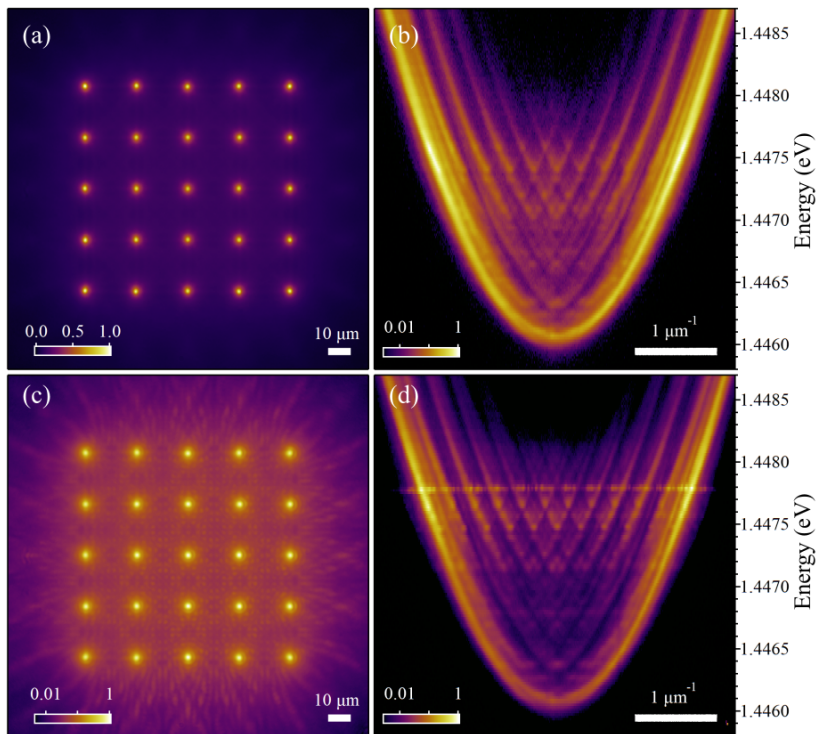


Figure S1. Optical lattice of 25 polariton condensates arranged in a square geometry with a lattice constant set to $D = 22.5 \mu\text{m}$. (a,c) Real space and (b,d) energy-resolved momentum space polariton PL at ($P \approx P_{\text{thr}}$) and above ($P \approx 1.3P_{\text{thr}}$) threshold respectively.

in momentum space becomes,

$$\hat{E}(\mathbf{k}) = \frac{1}{2} \left[\hat{E}_\phi(\mathbf{k}) - \sqrt{\hat{E}_\phi^2(\mathbf{k}) + (\hbar\Omega)^2} \right] \quad (\text{S2})$$

where $\hat{E}_\phi(\mathbf{k})$ is the cavity photon dispersion and $\hbar\Omega = 12$ meV is the Rabi energy. The confined photons obey,

$$\hat{E}_\phi(\mathbf{k}) = \sqrt{\left(\frac{\hbar c}{\lambda}\right)^2 + \left(\frac{\hbar c k}{n}\right)^2} + \Delta - \frac{i\hbar\gamma}{2}, \quad (\text{S3})$$

where $\lambda = 860$ nm is the cavity resonance, $n = 3.556$ is the cavity refractive index, $\Delta = -5$ meV is the cavity photon detuning from the exciton resonance, and $\gamma = 1/6$ ps⁻¹ is the cavity photon lifetime. The real part of the calculated dispersion is shown with a white dashed line plotted against the experimentally retrieved dispersion in Fig. S2(a). In Fig. S2(b) we show a schematic of the Lieb lattice and the three square sublattices denoted by their label A, B, C .

The potential $V(\mathbf{r})$ is directly proportional to the incident non-resonant laser intensity and can be written as a superposition of spatially separated Gaussians,

$$V(\mathbf{r}) = V_0 \sum_{n=1}^N \exp \left[-\frac{(x - x_n)^2 + (y - y_n)^2}{2w^2} \right]. \quad (\text{S4})$$

Here, N is the number of pumps in question and x_n, y_n are their coordinates, V_0 denotes the complex potential strength. $\text{Re}(V_0) > 0$ and $\text{Im}(V_0) > 0$ denote the blueshift and particle gain experienced by polaritons respectively due to their interactions with the laser generated background of non-condensed particles, and $w = 1.274$ μm is the RMS width of the pump spots corresponding to 3 μm FWHM. The width is slightly larger than that of the lasers (2 μm FWHM) to account for the finite diffusion of excitons in the reservoir from the laser spot.

The dispersion of Eq. (S1) can be numerically obtained through simple Monte-Carlo methods where an average is performed over the evolution of many random realizations of the particle wavefunction $\Psi(\mathbf{r})$. This method is particularly useful for potentials which lack the usual symmetries required by Bloch theorem to work and to estimate which bands sustain particles the longest if a non-Hermitian dissipation is added to the system (mimicking particle escaping from the cavity). In Figures S3-S5 we show the calculated dispersion for several lattice geometries relevant to the study.

BLOCH THEOREM

In this section we investigate the dispersion belonging to Eq. (S1) by applying Bloch analysis. The following equations were used to calculate Fig. 3(i) and Fig. 4(k) in the main text. For simplicity, we apply a parabolic

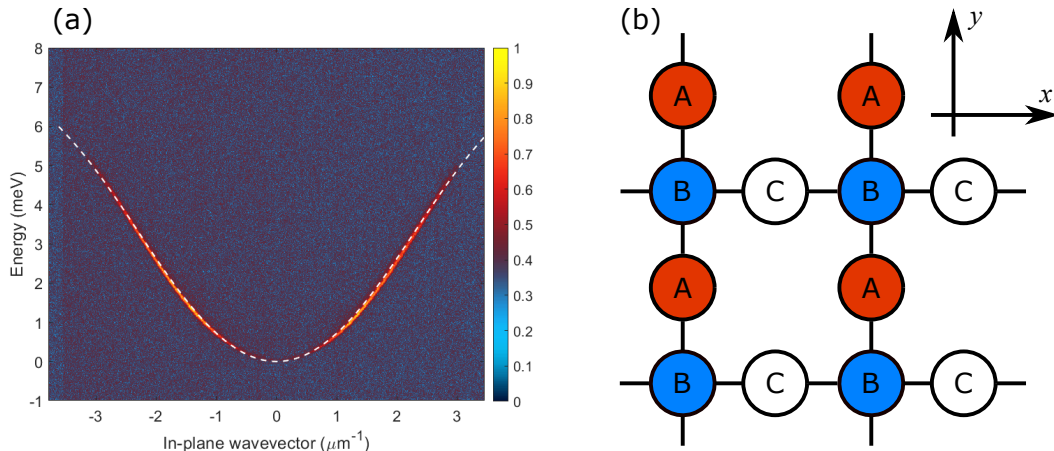


Figure S2. Bare lower polariton dispersion and Lieb lattice illustration. (a) Heatmap shows the normalized measured lower polariton dispersion with Eq. (S2) plotted on top as a white dashed line. (b) Schematic of the Lieb lattice geometry consisting of three square sublattices labeled A, B, C .

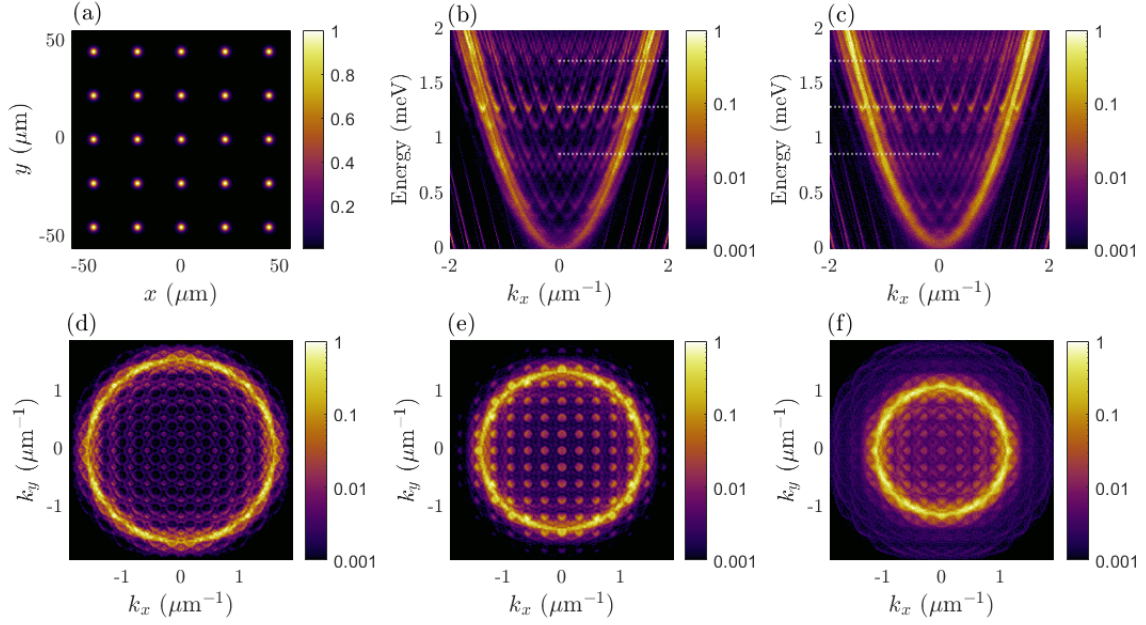


Figure S3. Calculated band structure in the polariton system in a square-shaped scatterer lattice of Gaussian potentials. (a) Non-resonant laser profile $V(\mathbf{r})$ (normalized) shaped into a square scatterer lattice of Gaussians with a lattice constant $D = 22.5 \mu\text{m}$ and $V_0 = 2 + 0.25i \text{ meV}$. (b,c) Energy-momentum space PL at (b) $k_y = 0$ and (c) $k_y = 2\pi/D$. (d-f) Polariton momentum space PL around threshold at $E = 1.72, 1.3, 0.87 \text{ meV}$ respectively corresponding to the dotted lines in (b,c).

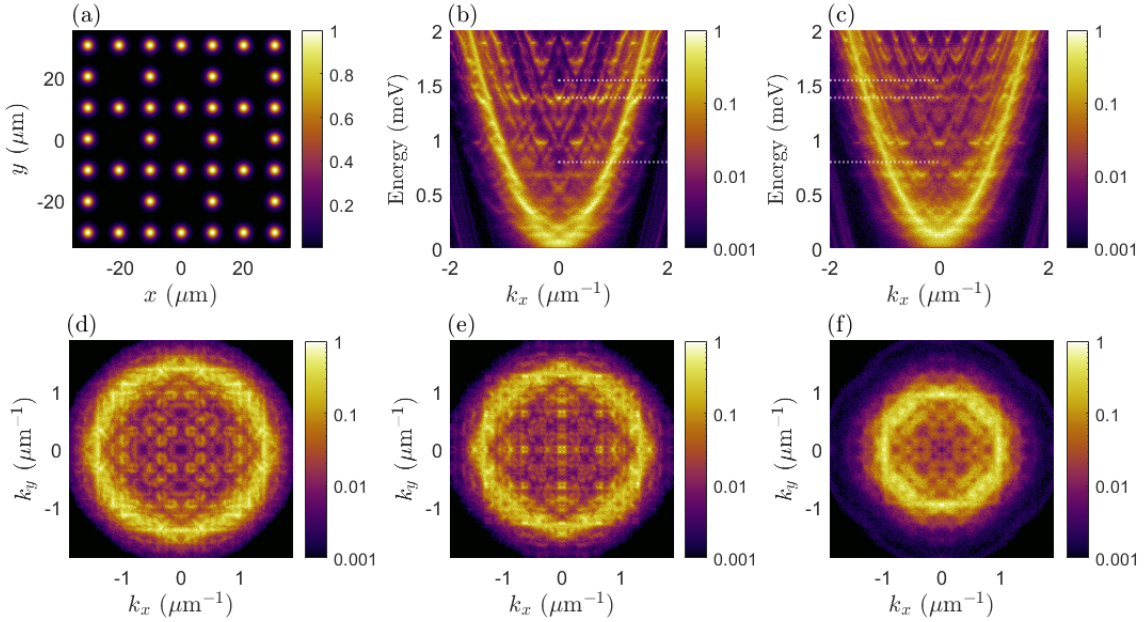


Figure S4. Calculated band structure in the polariton system in a Lieb-shaped scatterer lattice of Gaussian potentials. (a) Non-resonant laser profile $V(\mathbf{r})$ (normalized) shaped into a Lieb scatterer lattice of Gaussians with a lattice constant $D = 22.3 \mu\text{m}$ and $V_0 = 2.2 + 0.25i \text{ meV}$ corresponding to Fig. 3 in the main text. (b,c) Energy-momentum space PL around threshold for (b) $k_y = 0$ and (c) $k_y = 2\pi/D$. (d-f) Polariton momentum space PL around threshold at $E = 1.54, 1.38, 0.79 \text{ meV}$ respectively corresponding to the dotted lines in (b,c).

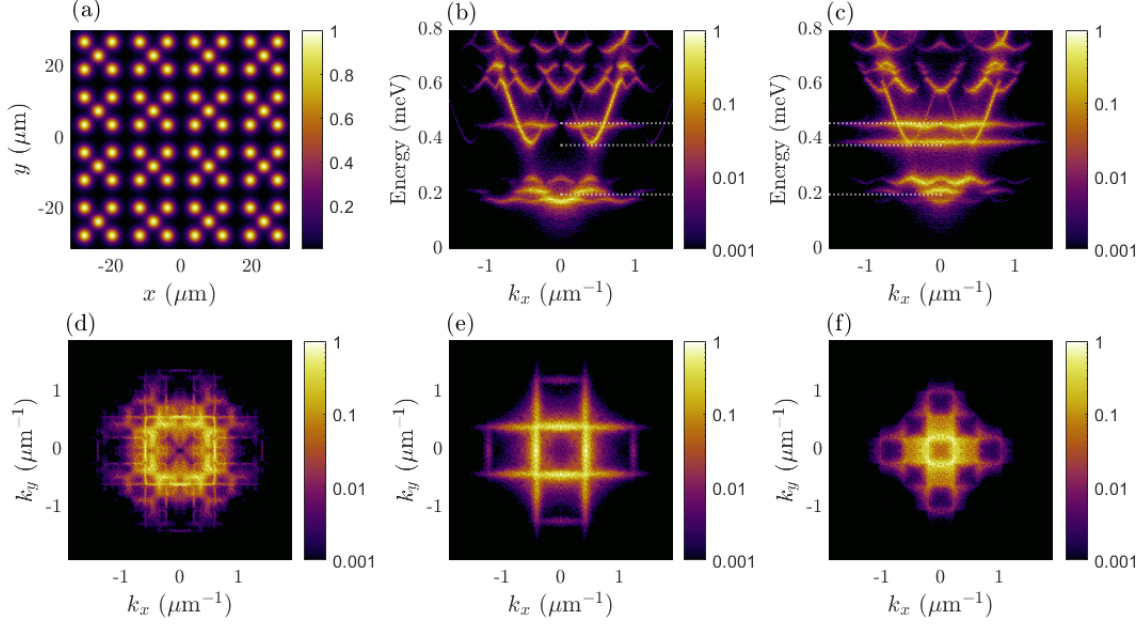


Figure S5. Calculated band structure in the polariton system in a Lieb lattice formed from inverse arrangement of Gaussian potentials. (a) Non-resonant laser profile shaped to form a conventional Lieb lattice of potential minima between the lasers. Lattice constant is $D = 15.6 \mu\text{m}$ and $V_0 = 2 \text{ meV}$ corresponding to Fig. 4 in the main text. (b,c) Energy-momentum space PL around threshold for (b) $k_y = 0$ and (c) $k_y = 2\pi/D$. (d-f) Polariton momentum space PL around threshold at $E = 0.47, 0.38, 0.2 \text{ meV}$ respectively corresponding to the dotted lines in (b,c).

approximation by writing,

$$\hat{E}(\mathbf{k}) = \frac{\hbar^2 k^2}{2m} \quad (\text{S5})$$

where the effective mass of the lower polaritons is $m = 0.32 \text{ meV ps}^2 \mu\text{m}^{-2}$. The potential is assumed to be infinite and periodic such that $V(\mathbf{r}) = V(\mathbf{r} + \mathbf{D})$ where $\mathbf{D} = n_1 \mathbf{a}_1 + n_2 \mathbf{a}_2$ is the translational symmetry vector defined in the bases of primitive lattice vectors $\mathbf{a}_{1,2}$ for some integers $n_{1,2}$. We can then apply Bloch's theorem where we write the polariton single particle wavefunction in the factorised form of crystal momentum $\mathbf{q} = (q_x, q_y)$ and Bloch states in the n th band $u_{n,\mathbf{q}}(\mathbf{r})$,

$$\Psi_n(\mathbf{r}) = e^{i\mathbf{q}\cdot\mathbf{r}} u_{n,\mathbf{q}}(\mathbf{r}). \quad (\text{S6})$$

Here, $u_{n,\mathbf{q}}(\mathbf{r}) = u_{n,\mathbf{q}}(\mathbf{r} + \mathbf{D})$. Substituting Eq. (S6) into Eq. (S1) the Bloch eigenvalue problem then reads,

$$\left[\frac{\hbar^2}{2m} \left[\left(q_x - i \frac{\partial}{\partial x} \right)^2 + \left(q_y - i \frac{\partial}{\partial y} \right)^2 \right] + V(\mathbf{r}) \right] u_{n,\mathbf{q}}(\mathbf{r}) = E_{n,\mathbf{q}} u_{n,\mathbf{q}}(\mathbf{r}). \quad (\text{S7})$$

We can diagonalise Eq. (S7) by expressing the Gaussian potential as a Fourier series in the basis of the reciprocal lattice vectors defined through $\mathbf{G} \cdot \mathbf{D} = 2\pi n$ for $n \in \mathbb{Z}$,

$$V(\mathbf{r}) = \sum_G V_G e^{i\mathbf{G}\cdot\mathbf{r}}. \quad (\text{S8})$$

Figure S6(a) shows a closer look at the calculated band structure for a scatterer Lieb lattice for $D = 22.3 \mu\text{m}$ with some features of interest marked with magenta colored boxes. Figure S6(b) shows the real space intensity of the Bloch state $|u_{n_c, \mathbf{q}=0}|^2$, marked by red circle, belonging to the pump-induced potential geometry $V(\mathbf{r})$ shown in Fig. S6(f). This state corresponds to the experimentally observed pattern shown in the inset of Fig. 2(b) in the main text. A portion of the Gaussian pump locations are marked by red squares for clarity.

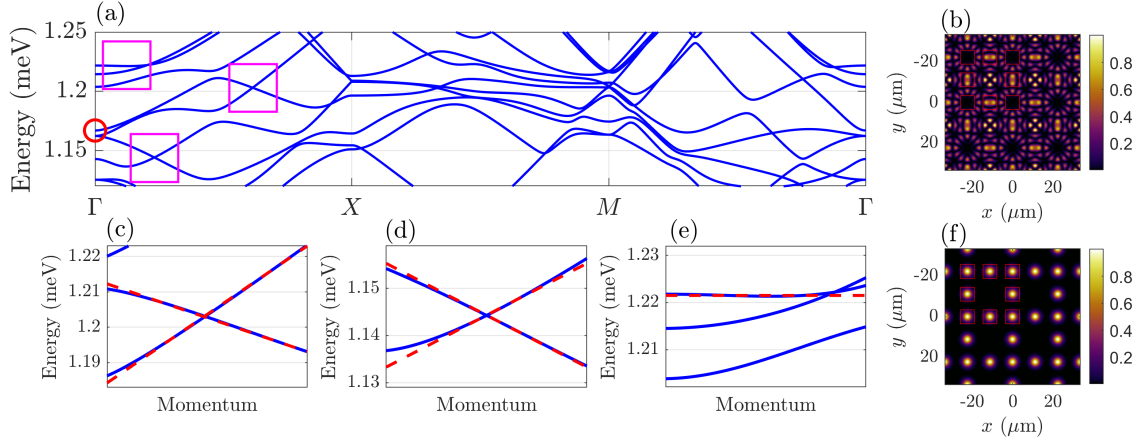


Figure S6. Closeup of the calculated band features appearing in the Lieb scatterer lattice. (a) Calculated bands using Eq. (S7) for a Lieb lattice of Gaussians, similar to Fig. S4 and Fig. 2 in the main text. (b) Calculated Bloch state intensity $|u_{n_c, \mathbf{q}=0}(\mathbf{r})|^2$ belonging to the band marked by the red circle in (a) and the condensate real space PL from Fig. 2(b) in the main text. The arrangement of the Gaussian pumps is indicated by the red squares. (c-e) Zoomed in regions of the dispersion showing exotic points where the dispersion becomes practically linear (massless polaritons) or flat (heavy polaritons). (f) Potential profile $V(\mathbf{r})$ (normalized) shaped into a Lieb scatterer lattice of Gaussians with a lattice constant $D = 22.3 \mu\text{m}$ and $V_0 = 1.25 \text{ meV}$.

We observe that the calculated Bloch state shown in Fig. S6(b) shows complete destructive interference at one of the sublattices whereas in experiment finite condensate density can be observed at this node. This means the state being occupied by the condensate becomes modified by the stimulated particle gain and overcomes the interference properties of the linear lattice waves. The studied optical potential platform and subsequent condensation of polaritons thus permits study on the balance between linear lattice physics against nonlinear effects such as the stimulated scattering into the condensate, polariton-polariton interactions, and polariton-reservoir interactions.

Moreover, in Fig. S6(a) we observe regions in the band structure with almost linear- and flat-like bands [magenta squares zoomed in Fig. S6(c-e)]. Although such exotic points were not experimentally investigated in this study, their theoretical prediction enhances the versatility and importance of the investigated scatterer Lieb lattice. Even if stimulated scattering of polaritons into such points via non-resonant excitation is infeasible they can still be excited using resonant lasers. This can potentially open up investigation into nonlinear transport properties of nearly massless or slow-light polaritons.

TIGHT BINDING TREATMENT

Here, we show qualitatively why condensation preferably occurs into a flatband P-orbital based by considering a tight-binding treatment of the P-orbital states. We consider only nearest neighbor coupling and negligible mixing with neighboring S- and D-orbitals. Being a scalar problem, we also do not consider the polarization degree of freedom of the polaritons. The bulk Hamiltonian in the basis of single particle, lattice site, creation and annihilation operators can be written,

$$\begin{aligned}
 \hat{H} = \sum_{n,m} & \left[(\hat{b}_{n,m}^{(x)})^\dagger [J_2(\hat{a}_{n,m}^{(x)} + \hat{a}_{n-1,m}^{(x)}) - J_1(\hat{c}_{n,m}^{(x)} + \hat{c}_{n,m-1}^{(x)})] + \text{h.c.} \right. \\
 & + (\hat{b}_{n,m}^{(y)})^\dagger [J_1(\hat{a}_{n,m}^{(y)} + \hat{a}_{n-1,m}^{(y)}) - J_2(\hat{c}_{n,m}^{(y)} + \hat{c}_{n,m-1}^{(y)})] + \text{h.c.} \\
 & + \epsilon_{a,x}(\hat{a}_{n,m}^{(x)})^\dagger \hat{a}_{n,m}^{(x)} + \epsilon_{b,x}(\hat{b}_{n,m}^{(x)})^\dagger \hat{b}_{n,m}^{(x)} + \epsilon_{c,x}(\hat{c}_{n,m}^{(x)})^\dagger \hat{c}_{n,m}^{(x)} \\
 & \left. + \epsilon_{a,y}(\hat{a}_{n,m}^{(y)})^\dagger \hat{a}_{n,m}^{(y)} + \epsilon_{b,y}(\hat{b}_{n,m}^{(y)})^\dagger \hat{b}_{n,m}^{(y)} + \epsilon_{c,y}(\hat{c}_{n,m}^{(y)})^\dagger \hat{c}_{n,m}^{(y)} \right]. \quad (\text{S9})
 \end{aligned}$$

Here, $\hat{a}_{n,m}^{(x,y)}$, $\hat{b}_{n,m}^{(x,y)}$, $\hat{c}_{n,m}^{(x,y)}$ denote the annihilation operators at sublattices A, B, C respectively [see Fig. S2], (n, m) denotes the site index of the corresponding sublattice, and (x, y) P-orbital lobe alignment along the two orthogonal coordinates x, y of the lattice. The operators obey bosonic commutation relation $[\hat{a}_{n,m}^{(\alpha)}, (\hat{a}_{n',m'}^{(\beta)})^\dagger] = \delta_{\alpha,\beta} \delta_{n,n'} \delta_{m,m'}$

